TIME-DEPENDENT SOLUTIONS OF VISCOUS INCOMPRESSIBLE FLOWS IN MOVING CO-ORDINATES

MOSHE ROSENFELD* AND DOCHAN KWAK

NASA Ames Research Center, Moffett Field, CA 94035, U.S.A.

SUMMARY

A time-accurate solution method for the incompressible Navier–Stokes equations in generalized moving co-ordinates is presented. A finite volume discretization method that satisfies the geometric conservation laws for time-varying computational cells is used. The discrete equations are solved by a fractional step solution procedure. The solution is second-order-accurate in space and first-order-accurate in time. The *pressure* and the *volume fluxes* are chosen as the unknowns to facilitate the formulation of a consistent Poisson equation and thus to obtain a robust Poisson solver with favourable convergence properties. The method is validated by comparing the solutions with other numerical and experimental results. Good agreement is obtained in all cases.

KEYS WORDS   Incompressible Navier–Stokes   Time-dependent   Moving co-ordinate systems   Finite volume Fractional step

1. INTRODUCTION

Numerous solutions have been obtained for steady incompressible flows in complicated three-dimensional configurations (see e.g. Reference 1). Time-dependent viscous flow simulations require large computational resources and only recently, with the advent of new and powerful supercomputers, has their solution becomes feasible for relatively complicated problems. The majority of the existing studies consider cases where a fixed grid can be employed. However, there are many realistic situations where one or more boundaries move, such as internal flows with a moving piston, biofluid flows with elastic boundaries or external flows over moving control surfaces of aircraft. Another example which requires the use of moving grids is the application of adaptive grids for computing time-dependent flow fields.

Several methods are being used for solving the incompressible Navier–Stokes equations over fixed grids (see e.g. References 1–4). The extension of these algorithms to the moving grid case is not trivial if time accuracy is required. Very few results, either numerical or experimental, are available for flow problems with varying geometry, especially in the case of incompressible flows. Ralph and Pedley[5] have solved the flow in a two-dimensional channel with a moving indentation using the streamfunction–vorticity method. They employed a specially devised time-dependent co-ordinate transformation to resolve the difficulties associated with the moving boundary. Their

---

* Permanent address: Department of Fluid Mechanics, Faculty of Engineering, Tel-Aviv University, Ramat Aviv 69978, Israel. Author to whom all correspondence should be addressed.

procedure is restricted to a particular class of problems and cannot be applied for cases with arbitrarily moving mesh points. Ogawa and Ishiguro[6] solved a two-dimensional model of the blood flow in a human ventricle and the external flow over an oscillating aerofoil by using moving grids in conjunction with a streamfunction–vorticity formulation. The extension of the stream-function vorticity formulation to three-dimensional cases is not straightforward. The primitive variable formulation is more promising for general three-dimensional problems. Rogers and Kwak[2] have recently extended their time-accurate artificial compressiblity solution procedure to moving grids. This method was used for solving the three-dimensional flow field in a model of the artificial heart developed by the Pennsylvania State University[7] and the flow through a tilting valve.[8]

The choice of the discretization procedure has an important effect on the accuracy of the solution in generalized co-ordinate systems. In the finite difference method used in all the above-mentioned works the motion of the grid is taken into account through the time derivative terms of the co-ordinate system. The geometric conservation equations are difficult to satisfy and an additional differential equation has to be solved for the conservation of the volume.[2] In the finite volume method the geometric quantities have clear meaning, such as the volume and the area of the faces of the computational cells. The geometric conservation laws which relate these quantities can be easily satisfied with favourable effects on the overall accuracy.

In the context of moving grids the preservation of the volume for time-varying geometries is of special importance for incompressible flows, where failing to satisfy these laws may be manifested in the form of artificial mass sources, with adverse effects on the accuracy, robustness and efficiency of the solution method.

In the present work a fractional step procedure developed previously by the present authors[3,9] for solving time-dependent, incompressible, viscous flows in generalized fixed co-ordinate systems is extended to moving grids. The integral formulation of the governing equations, the finite volume discretization procedure and the numerical solution phases are combined to yield an accurate solution method for complicated flow problems. Special attention is given to the satisfaction of the geometric conservation laws (both in space and time) in order to minimize the discretization error of complicated configurations.

2. FORMULATION

The equations governing the flow of isothermal, constant density, incompressible, viscous fluids in a time-varying control volume with surface area vector $\mathbf{S}(t)$ and volume $V(t)$ are the conservation of mass,

$$\frac{\mathrm{d}V}{\mathrm{d}t} + \oint_{\mathbf{S}(t)} \mathrm{d}\mathbf{S} \cdot (\mathbf{u} - \mathbf{v}) = 0, \tag{1}$$

and the conservation of momentum,

$$\frac{\mathrm{d}}{\mathrm{d}t} \int_{V(t)} \mathbf{u} \, \mathrm{d}V = \oint_{\mathbf{S}(t)} \mathrm{d}\mathbf{S} \cdot \bar{\mathbf{T}}, \tag{2}$$

where t is the time, $\mathbf{u}$ is the velocity vector, $\mathrm{d}\mathbf{S}$ is a surface area element and $\mathrm{d}V$ is a volume element. The surface element velocity resulting from the motion of the control volume is $\mathbf{v}$. For Newtonian fluids the stress tensor $\bar{\mathbf{T}}$ is given by

$$\bar{\mathbf{T}} = -(\mathbf{u} - \mathbf{v})\mathbf{u} - P\bar{\mathbf{I}} + \nu[\nabla\mathbf{u} + (\nabla\mathbf{u})^{\mathrm{T}}]. \tag{3}$$

The quantity $\bar{\mathbf{I}}$ is the identity tensor, $\nabla\mathbf{u}$ is the gradient of $\mathbf{u}$ and $(\cdot)^{\mathrm{T}}$ is the transpose operator. The pressure is P and v is the effective kinematic viscosity. The differences between the fixed and moving grid equations are included in the surface element velocity $\mathbf{v}$ and in the time dependence of the cell geometry (volume and surface area).

Special cases of the general conservation law relate certain geometric quantities. These relations are referred to as the 'geometrical conservation laws'.[10] In the case of a time-varying control volume the volume conservation equation requires

$$\frac{\mathrm{d}V}{\mathrm{d}t} - \oint_{S(t)} \mathrm{d}\mathbf{S}\cdot\mathbf{v} = 0, \tag{4}$$

where the term $\mathrm{d}\mathbf{S}\cdot\mathbf{v}$ represents the volume swept by the surface element $\mathrm{d}\mathbf{S}$ over the time increment $\mathrm{d}t$. Thus the mass conservation equation has a form identical to the fixed grid case,

$$\oint_{S(t)} \mathrm{d}\mathbf{S}\cdot\mathbf{u} = 0. \tag{5}$$

The usual finite difference approach is to transform equations (2) and (5) into a differential form. In the present work the integral formulation is maintained to facilitate the derivation of the finite volume equations.

3. DISCRETIZATION

3.1. Geometric quantities

A general non-orthogonal co-ordinate system (ξ, η, ζ) is defined (discretely) by

$$\mathbf{r} = \mathbf{r}(\xi, \eta, \zeta, t), \tag{6}$$

where $\mathbf{r} = (x, y, z)^{\mathrm{T}}$ is the Cartesian co-ordinate system and t is the time. The computational domain (ξ, η, ζ) is divided into uniform primary cells with a formal mesh size of $\Delta\xi = \Delta\eta = \Delta\zeta = 1$. The centre of each primary cell is designated by the indices, i, j, k. In the finite volume discretization approach the integral governing equations are approximated over the computational volumes in the *physical space*. The computational co-ordinates (ξ, η, ζ) may be regarded as a parametric description of the physical space, where the computational cell is an arbitrary hexahedron.

The face l of a cell is given by the vector (Figure 1)

$$\mathbf{S}^l = \frac{\partial\mathbf{r}}{\partial(l+1)} \times \frac{\partial\mathbf{r}}{\partial(l+2)}, \tag{7}$$

where the computational co-ordinates $l = \xi$, η or ζ are in a cyclic order and $\times$ is the cross product operator. For example, the face vector $\mathbf{S}^\xi$ is given by

$$\mathbf{S}^\xi = \frac{\partial\mathbf{r}}{\partial\eta} \times \frac{\partial\mathbf{r}}{\partial\zeta}.$$

The vector quantity $\mathbf{S}^l$ has the magnitude of the area of the face and a direction normal to it. The differential analogue is given by $\mathbf{S}^l = (1/J)\nabla l$, where J is the Jacobian of the inverse of the transformation (6) and ∇l is the contravariant base vector. The volume V of a cell is the inverse of the Jacobian J.
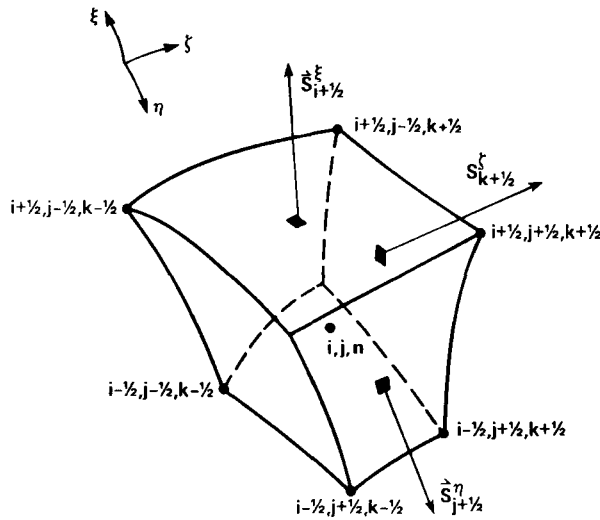
Figure 1. Definition of the primary cell

An accurate discretization should satisfy the geometric conservation laws.[3,9] These identities are derived as special cases of the general conservation laws (2) and (5) for a uniform velocity field. The accurate satisfaction of the discrete equations is required for minimizing the truncation errors related to generalized co-ordinate systems.

The condition that a cell is closed (a special case of (5)),

$$\oint_{S(t)} dS = 0,$$ (8)

should be satisfied exactly in the discrete form as well,

$$\sum_l S^l = 0,$$ (9)

where the summation is over all the faces of each computational cell. Equation (9) can be satisfied if S^l is computed from (7) by a proper approximation of $\partial r/\partial l$ (see details in Reference 3).

To ensure the discrete preservation of the total volume, the volume of each computational cell is computed by dividing it into three pyramids having in common the main diagonal and one vertex of the cell, resulting in the approximation

$$V = \tfrac{1}{3}(S_{i-1/2}^\xi + S_{j-1/2}^\eta + S_{k-1/2}^\zeta) \cdot (r_{i+1/2, j+1/2, k+1/2} - r_{i-1/2, j-1/2, k-1/2}).$$ (10)

For time-varying cells it is important to satisfy discretely the volume conservation equation (4). This can be accomplished by interpreting the term $dS \cdot v$ in equation (4) as the rate of the volume swept out by the face dS. For example, the volume swept out by the face $S_{i+1/2}^\xi$ can be computed by a formula similar to (10),

$$(\delta \mathscr{V}_{i-1/2}^\xi)^{n+1/2} = \tfrac{1}{3}[(S_{i-1/2}^\xi)^n + \delta S_{j-1/2}^\eta + \delta S_{k-1/2}^\zeta] \cdot (r_{i-1/2, j+1/2, k+1/2}^{n+1} - r_{i-1/2, j-1/2, k-1/2}^n),$$ (11)

where the time level is given by the superscript n. The quantities $\delta S_{j-1/2}^\eta$ and $\delta S_{k-1/2}^\zeta$ are the area vectors swept out by the motion of the face $S_{i-1/2}^\xi$—see the shaded surface in Figure 2. The area

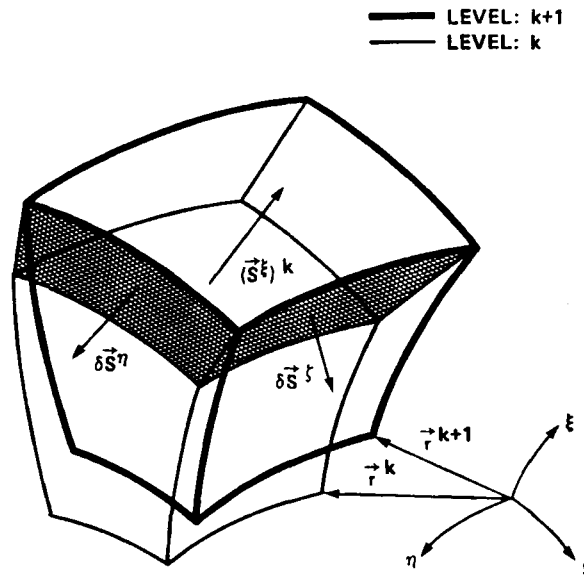Figure 2. Definitions related to moving grids

$\delta S^{\eta}_{j-1/2}$ is computed from

$$\delta S^{\eta}_{j-1/2} = \tfrac{1}{2}[(\mathbf{r}^{n+1}_{k-1/2} - \mathbf{r}^{n}_{k+1/2}) \times (\mathbf{r}^{n+1}_{k+1/2} - \mathbf{r}^{n}_{k-1/2})]_{i-1/2, j-1/2}, \tag{12}$$

and $\delta S^{\zeta}_{k-1/2}$ can be computed in a similar way. The volume of a cell at the time level $n+1$ is computed from (4):

$$V^{n+1} = V^{n} + \sum_{l} (\delta \mathscr{V}^{l})^{n+1/2}, \tag{13}$$

where the summation is over all the faces of the computational cell.

It is to be noted that $\delta \mathscr{V}^{l}/\Delta t$ is a volume flux due to the motion of the appropriate face of the control volume. A major difference between the finite volume and finite difference approaches involving moving grids is in the interpretation of this quantity. In the finite volume method it is treated as a geometric quantity whereas in the finite difference method the grid velocity (e.g. the velocity of the face of the computational cell) is combined with the fluid velocity to define a 'relative flow velocity'.[10]

In the present finite volume fomulation no co-ordinate derivatives appear in the discrete equations. Instead, quantities with clear geometric meaning, such as the volume and face area of the computational cells, are used. Their discrete approximation is based on geometric interpretations which satisfy the geometric conservation laws.

3.2. Mass conservation equation

The mass conservation equation (5) has the same form as for the fixed grid case. Discretization over the faces of the primary computational cells yields

$$(\mathbf{S}^{\xi} \cdot \mathbf{u})_{i+1/2} - (\mathbf{S}^{\xi} \cdot \mathbf{u})_{i-1/2} + (\mathbf{S}^{\eta} \cdot \mathbf{u})_{j+1/2} - (\mathbf{S}^{\eta} \cdot \mathbf{u})_{j-1/2} + (\mathbf{S}^{\zeta} \cdot \mathbf{u})_{k+1/2} - (\mathbf{S}^{\zeta} \cdot \mathbf{u})_{k-1/2} = 0. \tag{14}$$

Note that throughout the present paper the default indices (i, j, k) and the default time level $(n+1)$

are usually omitted for simplicity. Each term on the left-hand side of (14) approximates the volume flux over a face of the primary cell. A simple discretized mass conservation equation can be obtained by using the variables

$$U^\xi = \mathbf{S}^\xi \cdot \mathbf{u}, \qquad U^\eta = \mathbf{S}^\eta \cdot \mathbf{u}, \qquad U^\zeta = \mathbf{S}^\zeta \cdot \mathbf{u} \tag{15}$$

as the unknowns instead of the Cartesian velocity components $\mathbf{u}$. The quantities U^ξ, U^η and U^ζ are the volume fluxes over the ξ-, η- and ζ-faces of the primary cell respectively. In tensor algebra nomenclature these are the contravariant components of the velocity vector multiplied by a proper volume of each computational cell. With this choice of the dependent variables the continuity equation takes a form identical to the Cartesian case,

$$U^\xi_{i+1/2} - U^\xi_{i-1/2} + U^\eta_{j+1/2} - U^\eta_{j-1/2} + U^\zeta_{k+1/2} - U^\zeta_{k-1/2} = 0. \tag{16}$$

In fractional step solution methods the exact satisfaction of the discrete mass conservation equation is important for obtaining accurate solutions and is crucial for the convergence of the Poisson equation (see e.g. Reference 4). Therefore the simple form (16), which can be satisfied to round-off errors in any co-ordinate system, suggests that the volume fluxes are the 'natural' dependent variables in the context of fractional step methods in generalized co-ordinate systems. This choice complicates the discretization of the momentum equations but is important for obtaining a divergence-free velocity field in generalized co-ordinate systems.

3.3. Momentum conservation equation

Spatial discretization of the momentum conservation law (2) over a computational cell with volume V yields

$$\frac{\mathrm{d}}{\mathrm{d}t}(V\mathbf{u}) = \sum_l \mathbf{S}^l \cdot \bar{\mathbf{T}} = \mathbf{F}. \tag{17}$$

The arbitrary motion of the faces of the computational cell requires special considerations in the approximation of equation (17). First the discretization in time will be depicted.

Following the development of the fixed grid scheme given by Rosenfeld et al.,[3] a general two-step temporal discretization of (17) for a constant time step Δt is given by

$$(1+\varepsilon)(V\mathbf{u})^{n+1} - (1+2\varepsilon)(V\mathbf{u})^n + \varepsilon(V\mathbf{u})^{n-1} = \Delta t[\theta\mathbf{F}^{n+1} + (1-\theta)\mathbf{F}^n + \phi(\mathbf{F}^n - \mathbf{F}^{n-1})], \tag{18}$$

where ε, θ and ϕ are parameters to be selected for a particular scheme. A truncation error analysis shows that second-order accuracy in time is obtained only if

$$\tfrac{1}{2} + \varepsilon = \theta + \phi. \tag{19}$$

In the present study the dependent variables are the pressure defined at the centre of each primary cell and the volume fluxes defined on the faces of the primary cell. This choice requires the reformulation of the momentum equations in terms of the volume fluxes U^l. This can be done by a scalar multiplication of the vector momentum equations with the corresponding face vector $\mathbf{S}^l$, i.e. the momentum equation is projected onto the direction of each of the face vectors $\mathbf{S}^l$, $l = \xi, \eta, \zeta$.

The momentum equation for each component U^l is discretized over a different computational cell. Each cell has the formal size of $\Delta\xi \times \Delta\eta \times \Delta\zeta$ in the computational space but the centres are located at $(i+\tfrac{1}{2}, j, k)$, $(i, j+\tfrac{1}{2}, k)$ and $(i, j, k+\tfrac{1}{2})$ for the U^ξ-, U^η- and U^ζ-momentum equations respectively.
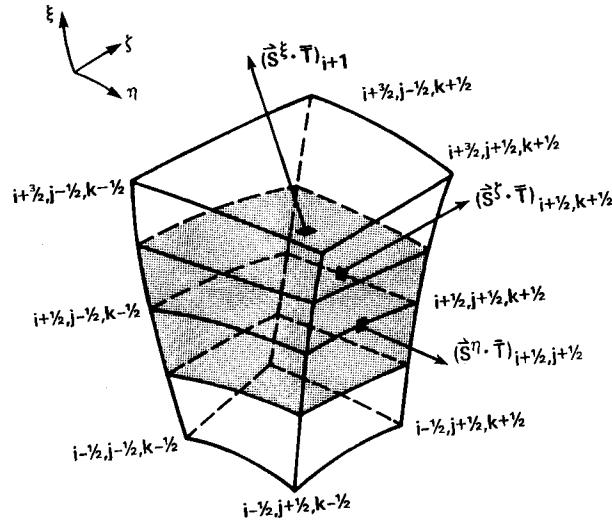
Figure 3. Definition of the U^ξ-momentum equation cell

The derivation of the ξ-momentum equation will be described in this subsection. The other two momentum equations can be obtained by cyclic permutation. The control volume used for the discretization of the ξ-momentum equation is shown in Figure 3 as the shaded region between two adjacent primary cells along the ξ-co-ordinate.

The Cartesian components of the velocity, **u**, can be substituted by the volume fluxes U^l by using the identity

$$\mathbf{u} = \mathbf{S}_\xi U^\xi + \mathbf{S}_\eta U^\eta + \mathbf{S}_\zeta U^\zeta = \mathbf{S}_m U^m. \tag{20}$$

The scalar momentum equation along the ξ-direction is obtained by a scalar multiplication of the vector momentum equation (18) with $\mathbf{S}^l$. Using (20), one obtains

$$(1+\varepsilon)(VU^\xi)^{n+1} - (1+2\varepsilon)(VU^l)^n(\mathbf{S}^\xi \cdot \mathbf{S}_l^n) + \varepsilon(VU^l)^{n-1}(\mathbf{S}^\xi \cdot \mathbf{S}_l^{n-1}) = \mathrm{RHS}, \tag{21}$$

where

$$\mathrm{RHS} = \Delta t [\theta \mathbf{S}^\xi \cdot \mathbf{F}^{n+1} + (1-\theta)\mathbf{S}^\xi \cdot \mathbf{F}^n + \phi \mathbf{S}^\xi \cdot (\mathbf{F}^n - \mathbf{F}^{n-1})].$$

The vector base $\mathbf{S}_m$ is the inverse base of $\mathbf{S}^l$. The $n+1$ is the default time level and therefore $\mathbf{S}^\xi$ is computed at $n+1$. To save computations and storage, the right-hand side of (21) is approximated as below such that only the term $L = \mathbf{S}^\xi \cdot \mathbf{F}$ at the time levels $n-1$, n and $n+1$ appears:

$$\begin{aligned}
\mathrm{RHS}/\Delta t &= \theta(\mathbf{S}^\xi \cdot \mathbf{F})^{n+1} + (1-\theta)(\mathbf{S}^\xi \cdot \mathbf{F})^n + \phi[(\mathbf{S}^\xi \cdot \mathbf{F})^n - (\mathbf{S}^\xi \cdot \mathbf{F})^{n-1}] \\
&= \theta L^{n+1} + (1-\theta)L^n + \phi(L^n - L^{n-1}).
\end{aligned} \tag{22}$$

By choosing $\varepsilon = \frac{1}{2}$ and $\phi = 1-\theta$, the above relation results in the following second-order-accurate scheme in time:

$$3(VU^\xi)^{n+1} - 4(VU^l)^n(\mathbf{S}^\xi \cdot \mathbf{S}_l^n) + (VU^l)^{n-1}(\mathbf{S}^\xi \cdot \mathbf{S}_l^{n-1}) = 2\Delta t[\theta L^{n+1} + (1-\theta)(2L^n - L^{n-1})]. \tag{23}$$

For numerical stability reasons, $\theta = 1$ was chosen in all the present calculations.

The computation of the operator L is similar to the fixed grid case. First, the vector flux is computed on each face of the computational cell. For example, the flux over the face ξ in the U^ξ-momentum equation (see Figure 3) is computed from (3):

$$(\mathbf{S}^\xi \cdot \bar{\mathbf{T}})_{i,j,k} = \left[-\left(U^\xi - \frac{\delta \mathscr{V}^\xi}{\Delta t} \right) U^l S_l - \mathbf{S}^\xi P + \mathbf{S}^\xi \cdot \nu [\nabla \mathbf{u} + (\nabla \mathbf{u})^T] \right]_{i,j,k}. \tag{24}$$

The conservative form of the velocity vector gradient is used:

$$\nabla \mathbf{u} = \frac{\oint_s d\mathbf{S} \mathbf{u}}{V}. \tag{25}$$

Applying (25) to the computation of $\nabla \mathbf{u}_{i,j,k}$ yields

$$\nabla \mathbf{u}_{i,j,k} = \frac{1}{V} (\mathbf{S}^\xi_{i+1/2} \mathbf{u}_{i+1/2} - \mathbf{S}^\xi_{i-1/2} \mathbf{u}_{i-1/2} + \mathbf{S}^\eta_{j+1/2} \mathbf{u}_{j+1/2} - \mathbf{S}^\eta_{j-1/2} \mathbf{u}_{j-1/2}$$

$$+ \mathbf{S}^\zeta_{k+1/2} \mathbf{u}_{k+1/2} - \mathbf{S}^\zeta_{k-1/2} \mathbf{u}_{k-1/2})$$

$$= \frac{1}{V} (\mathbf{S}^\xi_{i+1/2} \mathbf{S}_{l,i+1/2} U^l_{i+1/2} - \mathbf{S}^\xi_{i-1/2} \mathbf{S}_{l,i-1/2} U^l_{i-1/2} + \mathbf{S}^\eta_{j+1/2} \mathbf{S}_{l,j+1/2} U^l_{j+1/2}$$

$$- \mathbf{S}^\eta_{j-1/2} \mathbf{S}_{l,j-1/2} U^l_{j-1/2} + \mathbf{S}^\zeta_{k+1/2} \mathbf{S}_{l,k+1/2} U^l_{k+1/2} - \mathbf{S}^\zeta_{k-1/2} \mathbf{S}_{l,k-1/2} U^l_{k-1/2}). \tag{26}$$

The fluxes at the point (i, j, k) are computed by a regular averaging and therefore the scheme is equivalent to second-order central differences. The η- and ζ-face centres are at $(i+\frac{1}{2}, j-\frac{1}{2}, k)$ and $(i+\frac{1}{2}, j, k-\frac{1}{2})$ respectively. The fluxes over these faces are computed in a similar way.

One major difference between the moving grid and the fixed grid discretization is in computing the convection terms which include the motion of the grid. For example, the ξ-face flux of the ξ-momentum equation originating from the convection terms is given by (see (24))

$$\left[-\left(U^\xi - \frac{\delta \mathscr{V}^\xi}{\Delta t} \right) U^l S_l \right]_{i,j,k}.$$

In the present implementation the computation of $\delta \mathscr{V}^\xi$ lags in time by $\Delta t/2$ and therefore the resulting scheme is first-order-accurate in time.

The scheme is spatially second-order-accurate. For high-Reynolds-number flows, fourth-order dissipation may be added to annihilate high-frequency components of the solution without degrading the second-order spatial accuracy.

It should be noted that in the present finite volume discretization method the explicit evaluation of complicated Cristoffel symbols is not required, unlike in the case of finite difference formulations that use the contravariant components of the velocity as the dependent variables.

4. SOLUTION METHOD

The mass and momentum conservation equations are solved by a fractional step method.[3, 9] First the momentum equations are solved for an approximate U^l by an approximate factorization technique using the pressure from the previous time level. In the second stage the pressure and the volume fluxes U^l are corrected to satisfy the mass conservation equation by solving a Poisson equation.

The solution of the resulting Poisson equation with Neumann-type boundary conditions requires careful attention to the proper discrete formulation to ensure the existence of a solution.

The present selection of the dependent variables and the definition of the pressure at the centre of each computational cell ensures the existence of a solution of the Poisson equation with favourable effects on the convergence properties of the Poisson solver. No modification of the source terms is required and therefore the mass conservation equation can be satisfied to machine accuracy. Additional details on the solution method can be found in References 3 and 9.

The fixed grid method used an explicit approximation of the convection terms. In the present implementation the convection terms may be approximated also implicitly and therefore the scheme has no severe restrictions on the allowable CFL number. Explicit or implicit fourth-order dissipation can be used for high-Reynolds-number flows and the boundary conditions may be of Dirichlet, Neumann or periodic type.

5. RESULTS

The main purpose of this section is to validate the suggested method for solving the time-dependent Navier–Stokes equations in generalized moving co-ordinate systems. It is not intended to study new cases that have not been previously considered. The basic features of the algorithm are equally applicable to both two- and three-dimensional cases. The computer code is written for general three-dimensional flow problems, but so far only two-dimensional cases have been considered.

5.1. Flow over a circular cylinder

The flow field over a circular cylinder at $Re = 40$ was solved as the first test case. This example is frequently used for validating fixed grid solution methods because the resulting flow field offers rich fluid dynamic phenomena and other numerical and experimental results are available for comparison. In the present case a radially expanding grid is generated by choosing a moving circular outer boundary. The distance R_{max} of the outer boundary from the centre of the cylinder is specified by

$$R_{max}(t) = 7 + \frac{4t}{3} - \frac{t^2}{24},\qquad(27)$$

where t is the time and the distance R_{max} is normalized by the diameter of the circular cylinder. A cylindrical co-ordinate system is used with mesh points clustered near the cylinder and in the wake region. The above relation results in a significant radial grid velocity relative to the flow velocity in the wake region.

Figure 4 gives the grid and the instantaneous streamlines for $t = 1$ and 8. Figure 5 compares the time evolution of the separation bubble, which a critical test parameter, with the experimental result of Bouard and Coutanceau[11] and the numerical computations of Collins and Dennis[12] (using a fixed grid). The results obtained from the fixed grid version of the present method are also given. Very good agreement is obtained and practically all the results coincide. The discrepancy of the numerical results of Reference 12 for $t > 7$ may be attributed to the location of the outer boundary. Note especially the good agreement with the experimental results which have been obtained for an equivalent outer boundary of about 14 diameters. This is about the same as the outer boundary distance in the present computations at $t \approx 8$.

5.2. Channel flow with an asymmetric oscillating indentation

The next validation case simulates the laminar flow in a two-dimensional channel with an oscillating constriction. This models the large-amplitude self-excited oscillations that arise when

$$T = 1 \quad , \quad R_{max} = 8.29$$
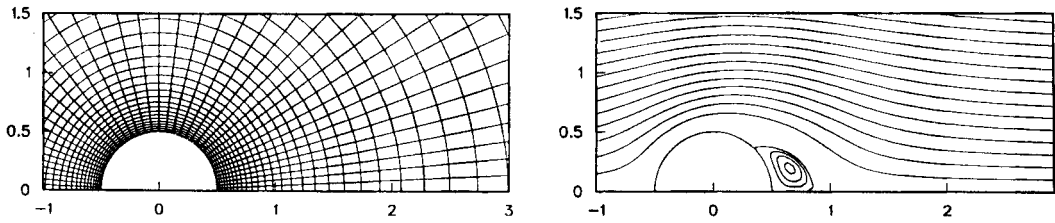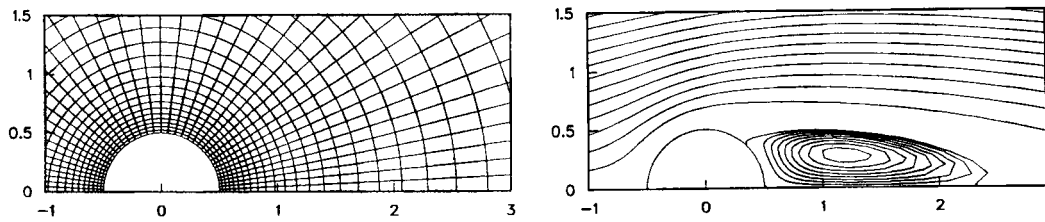

$$T = 8 \quad , \quad R_{max} = 15.00$$

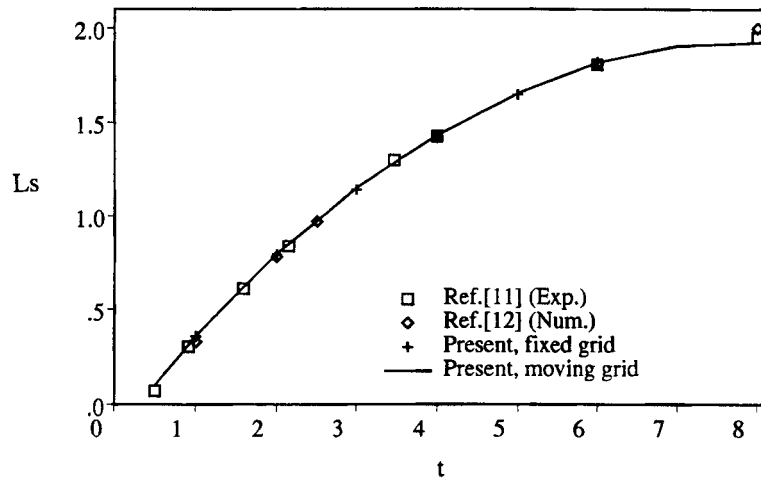Figure 4. Grid and instantaneous streamline contours for $t = 1$ and 8

Figure 5. Time evolution of separation length over a circular cylinder at $Re = 40$

fluid flows through a collapsible tube such as a vein. In a series of flow visualizations, Stephanoff et al.[13] and Pedley and Stephanoff[14] have found a complicated flow structure downstream of the oscillating indentation. A train a waves was found in the core flow along with a double row of counter-rotating eddies along both walls of the channel.

In the experimental apparatus the walls of the channel were rigid except for an indentation of length 10 (the distance between the fixed parts of the two walls is the reference unit length). The channel starts at a distance of 120 units upstream of the oscillating constriction and is 250 units long. The indentation is made of a thick rubber membrane and is driven by a piston with a sinusoidal motion in time and a maximal indentation of 0·38 units. At the beginning of each cycle the indentation is flushed with the wall of the channel.

In the present numerical work a simplified model of the test apparatus is used. The upstream boundary is at a distance of 5 units from the oscillating constriction and the downstream boundary is at a distance of 30 units from the upstream boundary. An algebraic grid is generated at each time step with $31 \times 251 \times 3$ points along the height, length and width of the channel respectively (at least three points are required in the third direction to compute two-dimensional flows with the three-dimensional code). Points are clustered near the two solid walls and a non-uniform distribution of points is used in the axial direction with clustering in the region downstream of the indentation, where the flow structure was found experimentally to be the most interesting. The mesh points are fixed in time except at the indentation region, where they stretch linearly with the distance between the moving indentation and the opposite fixed wall. The grid at the midpoint of the cycle, when the identation is maximal, is shown in Figure 6 (only every other point is plotted in the normal and axial directions and the vertical scale is twice as large as the axial scale). The shape of the indentation is approximated by a hyperbolic tangent, as has been suggested by Pedley and Stephanoff[14] (the apparent asymmetry of the indentation in Figure 6 is a result of the non-uniform grid). Several numerical experiments revealed the insensitivity of the flow downstream of the indentation of the upstream boundary conditions as well as to the upstream and downstream boundaries locations which were used in the present simulation.

Fully developed flow is given as the initial condition and at the upstream boundary. At the downstream boundary a non-reflective condition is imposed. At the upper and lower walls the velocity of the wall is specified (zero everywhere, except at the moving indentation).

Figure 7 shows a comparison of the instantaneous streamlines with a flow visualization of Stephanoff et al.[13] at the non-dimensional time of $t = 0·55$ (based on the period) for a case with a Strouhal number $St = 0·038$ and a Reynolds number $Re = 610$, based on the height of the channel and the average input velocity. The flow visualization shows quite a complicated flow field, although the resolution of the photograph is not good enough for revealing the fine details, especially in the regions of the eddies. The first separation of the flow occurs downstream of the sloping wall. A second large eddy is formed on the opposite wall with a secondary separation bubble buried inside it. Still further downstream an additional pair of weaker vortices appears, one on each wall. The core of the flow prescribes a wave motion which can be observed easily both in the experimental and the numerical results.

Favourable agreement can be obtained if the plot of the numerical results is shifted about 0·4 units of the channel's height in the downstream direction relative to the experimental results. It seems that the separation length of the first eddy at the upper wall is underpredicted in the present
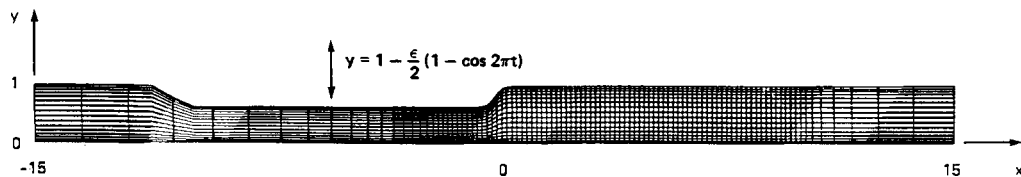

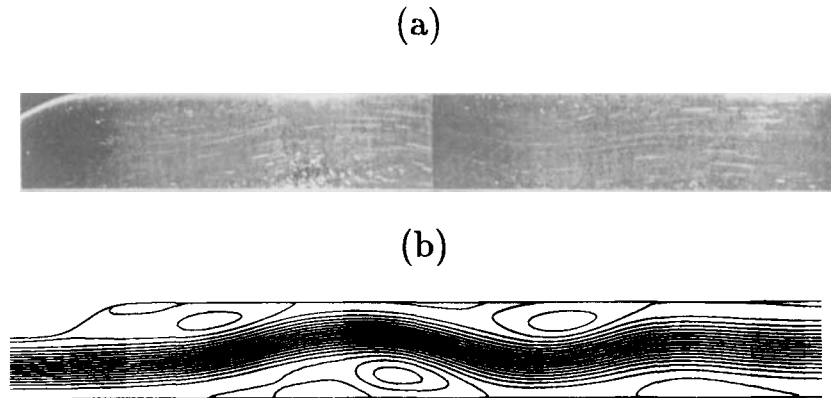Figure 6. Grid for channel flow with an oscillating indentation

(a)

(b)

Figure 7. Comparison of instantaneous streamlines at $t=0.55$ and $St=0.038$, $Re=610$: (a) experimental results; (b) present results

computation. Nevertheless, the distance between the vortices, which are related to the wavelength of the core flow, compare favourably.

The reason for this discrepancy is not clear. The differences do not seem to be related to the mesh resolution, since a grid refinement study has demonstrated that the present solution is practically grid-independent. Kiris and Rogers[15] have solved the same case using the artificial compressibility method with a high-order upwind scheme and found results similar to the present computations (see below). The fact that two numerical procedures which differ in numerous computational aspects results in similar solutions can indicate that the differences might be related to the modelling of the experimental set-up and the physical conditions. Another possible reason may be attributed to three-dimensional effects. In the present computations a two-dimensional flow is assumed. In the experiments conducted by Pedley and Stephanoff[14] the width of the channel was 10 times larger than its height. The three-dimensional affects of the side walls on the centre plane, where the visualizations were taken, could not be assessed. Armaly et al.[16] have investigated experimentally the steady flow past a backward-facing step and found three-dimensional effects for $Re>400$. The most sensitive quantity was the length of the main separation eddy behind the step. In unsteady flows the three-dimensional effects are usually even more pronounced (see e.g. Reference 17). Another reason for the disagreement could be the inaccurate description of the wall shape in the numerical computations. Obviously, any difference in the shape may affect the length of the separation from the indentation.

The flow evolution over one complete cycle is given in Figure 8 for $Re=600$ and a higher Strouhal number, $St=0.057$. The instantaneous streamlines are plotted at several instances (scaled by the period) over one complete cycle of the indentation. The flow development is remarkably similar to that found experimentally by Pedley and Stephanoff[14] and is summarized only briefly here. At the beginning of the cycle, during which the identation moves downwards' the downstream flow is accelerating, a single separation bubble forms on the sloping wall of the indentation (Figure 8(a)) and the core flow remains parallel to the walls. As time progresses, the separation length increases and a second counter-rotating eddy appears on the opposite wall, downstream of the first eddy (Figure 8(b)). The flow field is significantly changed during the second half of the period, when the indentation moves upwards and causes the deceleration of the flow downstream. A third eddy is formed at the upper wall further downstream at $t=0.55$
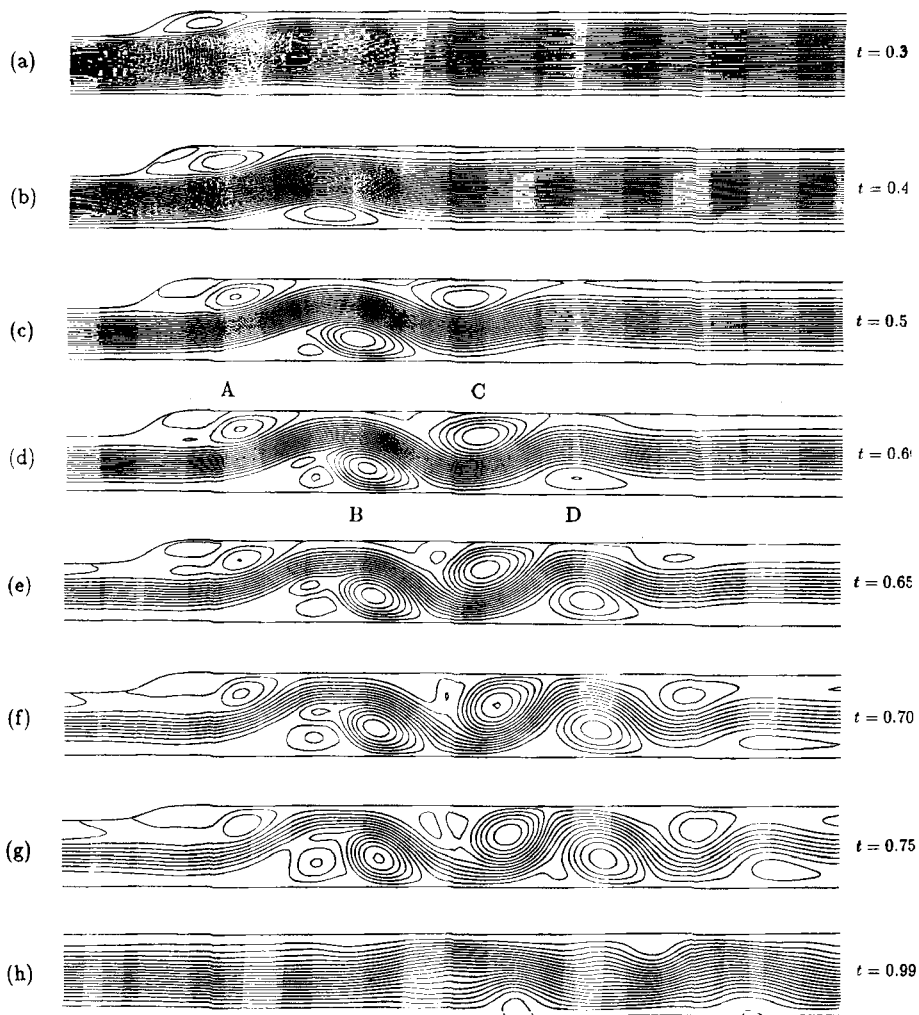
Figure 8. Instantaneous streamlines, $St = 0.057$, $Re = 600$

(Figure 8(c)). In the third quarter of the period the core flow becomes wavy and a sequence of eddies appears along the walls. The amplitude of the core flow increases with time until $t = 0.75$ (Figure 8(g)), which corresponds to the maximal deceleration. In the last quarter of the period the eddies shrink in size and strength and are washed downstream. At the end of the cycle the residual eddies are quite small and were found not to affect the next cycle. We shall adopt the convention of Reference 14 in labelling the eddies alphabetically as shown in Figure 8(d).

Of particular interest is the phenomenon of eddy doubling which was found experimentally in Reference 14. In this phenomenon a single eddy apparently splits into two *co-rotating* eddies. The present calculations show that eddy doubling occurs for eddies A, B and C for $t > 0.55$. The genesis of the wavy flow as well as the mechanism of the eddy doubling are still not fully understood. *Most previous studies agree that the wavy core flow is determined primarily by* inviscid vorticity dynamics and is a result of the non-vanishing vorticity gradient.[14, 17] It is also

clear that the eddy doubling is essentially a viscous phenomenon.[14] The motivation of the present paper is to describe and validate the numerical solution procedure; therefore no further attempt will be made to analyse the flow field at this time.

Figure 9 compares the time evolution of the centre of the vortices A, B, C and D (which approximately coincides with the crests and troughs of the core flow streamlines) with the numerical solution of Kiris and Rogers[15] and the experimental results of Pedley and Stephanoff.[14] The agreement between the two numerical results is good, except for slight discrepancies at the first separation eddy (A). The location of the first eddy, A, does not compare very well between the numerical and the experimental results, yet the *distances* between the vortices (the wavelength) compare favourably between all the results. This behaviour is similar to what was found in the discussion on Figure 7.

5.3. Internal flow driven by a piston

The last test case is included to demonstrate some of the capabilities of the present numerical procedure. In this case a two-dimensional internal flow in a rectangular cavity driven by a vertically oscillating piston is solved for a Reynolds number of 100. This flow field may be an idealization of the flow in a reciprocal engine. The geometry of the problem is given in Figure 10. The piston is moving sinusoidally between $y=0.6$ and $y=0.3$ with a period of 1.2 non-dimensional seconds. During the downward stroke of the piston the fluid leaves through an exit at the left vertical wall, and during the upward motion the entrance at the right vertical wall opens and the exit is closed.

An algebraic rectangular grid with $49 \times 45 \times 3$ points in the x-, y- and z-directions respectively has been generated. Mesh points are clustered near the two side walls and near the lower wall. Along the y-direction the mesh points are stretched linearly with the motion of the piston. The x-direction distribution remains fixed. Figure 11 shows the time evolution of the force coefficients in the y- and x-directions on the lower stationary horizontal wall (opposing the piston). A fully
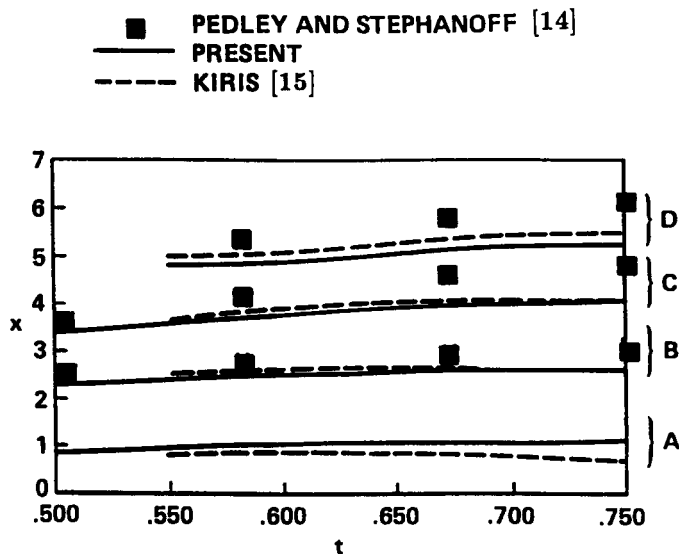

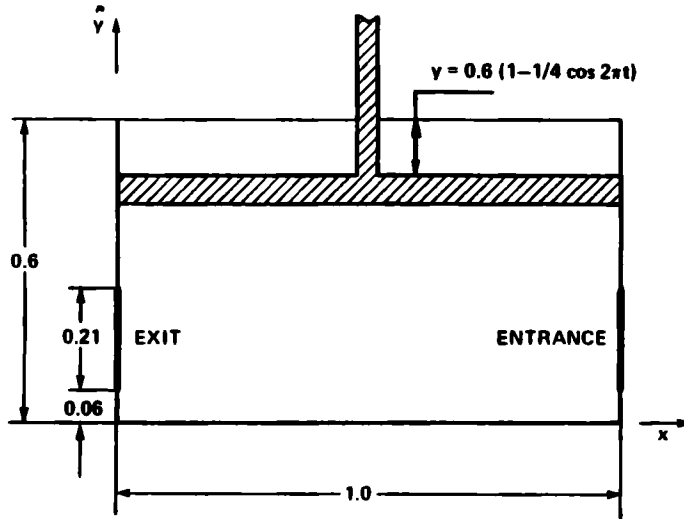Figure 9. Time evolution of centre of vortices
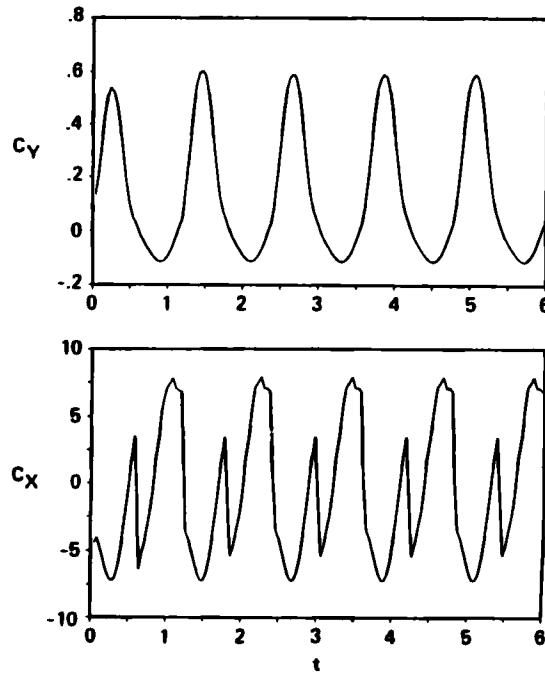
Figure 10. Geometry of piston flow case

Figure 11. Time evolution of force coefficients on lower wall

developed periodic flow is obtained beginning from the second cycle of the piston. The abrupt opening of the exit (at $t = 0.6$, 1.8, 3, etc.) and the abrupt closing of the entrance (at $t = 1.2$, 2.4, 3.6, etc.) can be clearly observed as sharp changes in the x-component of the force coefficient.
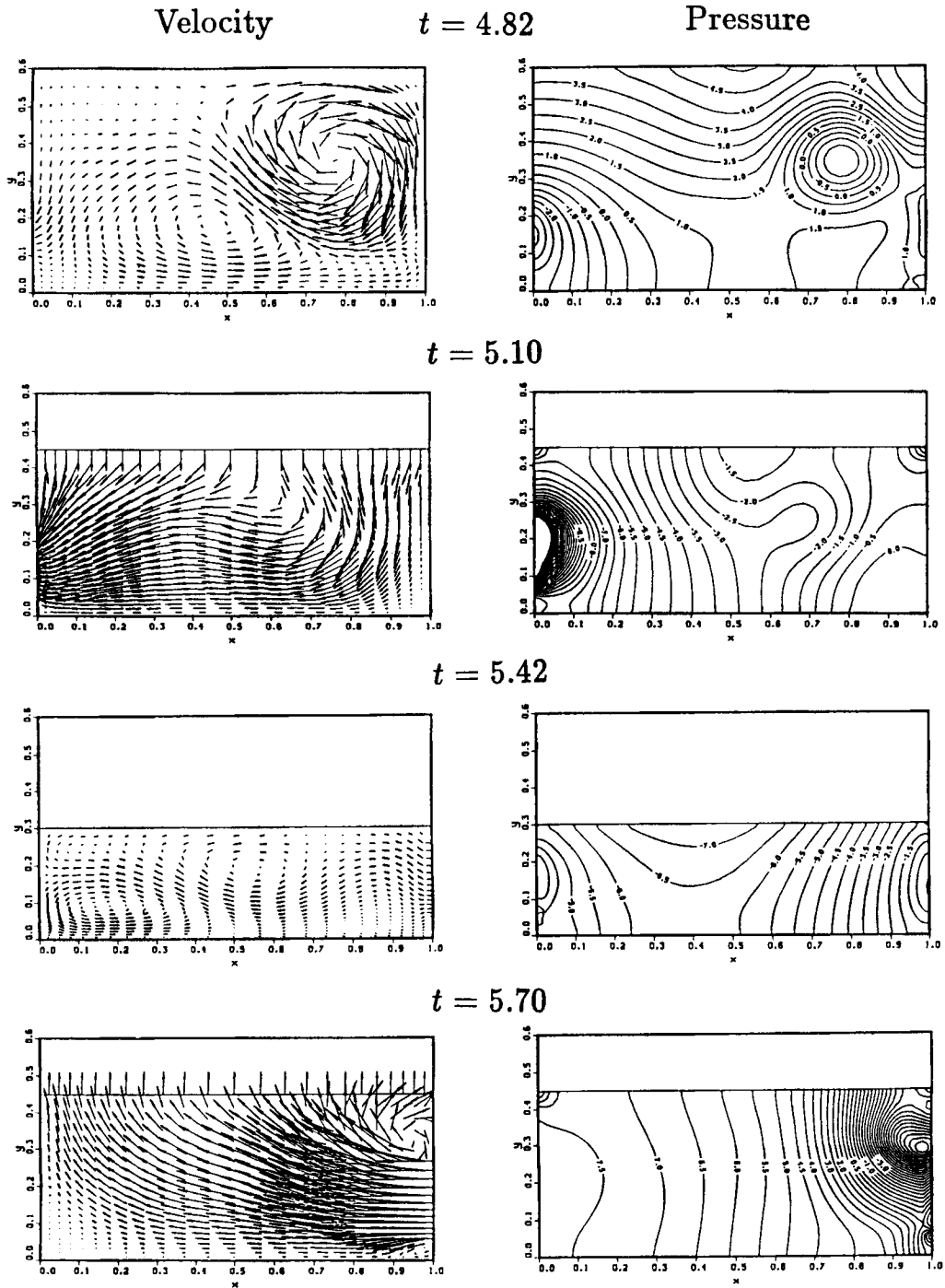
Figure 12. Velocity vectors and pressure contours

Figure 12 gives the velocity vector and the pressure contours for the fifth cycle. The velocity vector is plotted for every other mesh point in both the x- and y-directions. At the beginning of each cycle a strong vortex, which was created in the previous cycle, is found near the entrance, along with a counter-rotating weaker vortex. At half-stroke downward no vortices exist (except very weak vortices near the two lower corners) and a very strong pressure gradient builds up at the exit. As the entrance opens (Figure 12(c)), two main vortices are found in the core region, but they are weaker than the vortices at the beginning of the cycle. During the upward motion of the piston the strong vortex is regenerated near the entrance (Figure 12(d)).

A favourable agreement has been found with the numerical results of Kiris and Rogers,[15] who have solved the same case with a time-accurate artitificial compressibility method.

6. CONCLUDING REMARKS

A solution method for the time-accurate incompressible Navier–Stokes equations in a generalized curvilinear moving co-ordinate system has been presented. The choice of the *volume fluxes* as the dependent variables and the staggered location of the pressure ensured the satisfaction of the discrete mass conservation equation and permitted the formulation of a robust and efficient Poisson solver. Accuracy is achieved by employing finite volume discretization with special attention to the preservation of the geometric conservation laws in generalized *moving* coordinate systems. A fractional step solution method is used to solve the discrete equations.

Several test solutions demonstrated good agreement with other experimental and numerical results. Future work will include the solution of three-dimensional cases with moving boundaries as well as time-dependent problems with adaptive grids.

REFERENCES

1. D. Kwak, J. L. C. Chang, S. E. Rogers and M. Rosenfeld, 'Three-dimensional incompressible Navier–Stokes computations in internal flows', *Proc. 12th IMACS World Congr. on Scientific Computation*, Paris, 18–22 July 1988; also *NASA TM 100076*, March 1988.
2. S. E. Rogers and D. Kwak, 'Numerical solution of the incompressible Navier–Stokes equations for steady-state and time-dependent problems', *AIAA Paper 89-0463*, 1989.
3. M. Rosenfeld, D. Kwak and M. Vinokur, 'A solution method for the unsteady and incompressible Navier–Stokes equations in generalized coordinate systems', *AIAA Paper 88-0718*, 1988.
4. P. M. Gresho and R. L. Sani, 'On pressure boundary conditions for incompressible Navier–Stokes equations', *Int. j. numer. methods fluids*, **7**, 1111–1145 (1987).
5. M. E. Ralph and T. J. Pedley, 'Flow in a channel with a moving indentation', *J. Fluid Mech.*, **190**, 87–112 (1988).
6. S. Ogawa and T. Ishiguro, 'A method for computing flow fields around moving bodies', *J. Comput. Phys.*, **69**, 49–68 (1987).
7. S. E. Rogers, P. Kutler, D. Kwak and C. Kiris, 'Numerical simulation of flow through an artificial heart', *NASA TM 102183*, 1989.
8. C. Kiris, I. D. Chang, S. E. Rogers and D. Kwak, 'Numerical simulation of the incompressible internal flow through a tilting valve', *AIAA Paper 90-0682*, 1990.
9. M. Rosenfeld, D. Kwak and M. Vinokur, 'A fractional step solution method for the unsteady incompressible Navier–Stokes equations in generalized coordinate systems', *J. Comput. Phys.*, in the press.
10. M. Vinokur, 'An analysis of finite-difference and finite-volume formulations of conservation laws', *J. Comput. Phys.*, **81**, 1–52 (1989).

11. R. Bouard and M. Coutanceau, 'The early stage of development of the wake behind an impulsively started cylinder for $40 < Re < 10^4$', *J. Fluid Mech.*, **101**, 583–607 (1980).
12. W. M. Collins and S. C. R. Dennis, 'Flow past an impulsively started circular cylinder', *J. Fluid Mech.*, **60**, 105–127 (1973).
13. K. D. Stephanoff, T. J. Pedley, C. J. Lawrence and T. W. Secomb, 'Fluid flow along a channel with an asymmetric oscillating constriction', *Nature*, **305**, 692–695 (1983).
14. T. J. Pedley and K. D. Stephanoff, 'Flow along a channel with a time-dependent indentation in one wall: the generation of vorticity waves', *J. Fluid Mech.*, **160**, 337–367 (1985).
15. C. Kiris and S. E. Rogers, Private communication, September 1988.
16. B. F. Armaly, F. Durst, J. C. T. Pereira, and B. Schonung, 'Experimental and theoretical investigation of backward-facing step flow', *J. Fluid Mech.*, **127**, 473–496 (1983).
17. I. J. Sobey, 'Observation of waves during oscillatory channel flow', *J. Fluid Mech.*, **151**, 395–426 (1985).